2005

Time-dependent whole-body fluorescence tomography of probe bio-distributions in mice

Sachin V. Patwardhan
Washington University School of Medicine in St. Louis

Sharon R. Bloch
Washington University School of Medicine in St. Louis

Samuel Achilefu
Washington University School of Medicine in St. Louis

Joseph P. Culver
Washington University School of Medicine in St. Louis

Time-dependent whole-body fluorescence tomography of probe bio-distributions in mice

Sachin V. Patwardhan, Sharon R. Bloch, Samuel Achilefu, and Joseph P. Culver*

Mallinckrodt Institute of Radiology, Department of Radiology, Washington University School of Medicine, St. Louis, MO 63110.
culverj@wustl.edu

Abstract: We present a fast scanning fluorescence optical tomography system for imaging the kinetics of probe distributions through out the whole body of small animals. Configured in a plane parallel geometry, the system scans a source laser using a galvanometer mirror pair (τ_{switch}~1ms) over flexible source patterns, and detects excitation and emission light using a high frame rate low noise, 5 MHz electron multiplied charge-coupled device (EMCCD) camera. Phantom studies were used to evaluate resolution, linearity, and sensitivity. Time dependent (δ_t=2.2 min.) in vivo imaging of mice was performed following injections of a fluorescing probe (indocyanine green). The capability to detect differences in probe delivery route was demonstrated by comparing an intravenous injection, versus an injection into a fat pocket (retro orbital injection). Feasibility of imaging the distribution of tumor-targeted molecular probes was demonstrated by imaging a breast tumor-specific near infrared polypeptide in MDA MB 361 tumor bearing nude mice. A tomography scan, at 24 hour post injection, revealed preferential uptake in the tumor relative to surrounding tissue.

OCIS codes: (110.6960) Tomography; (260.2510) Fluorescence.

References and Links

1. Achilefu, S., R.B. Dorshow, J.E. Bugaj and R. Rajagopalan, "Novel receptor-targeted fluorescent contrast agents for in vivo tumor imaging," Invest. Radiol. **35,** 479-485 (2000).
2. Bremer, C., S. Bredow, U. Mahmood, R. Weissleder and C.H. Tung, "Optical imaging of matrix metalloproteinase-2 activity in tumors: Feasibility study in a mouse model," Radiol. **221,** 523-529 (2001).
3. Bugaj, J.E., S. Achilefu, R.B. Dorshow and R. Rajagopalan, "Novel fluorescent contrast agents for optical imaging of in vivo tumors based on a receptor-targeted dye-peptide conjugate platform," J. Biomed. Opt. **6,** 122-133 (2001).
4. Pogue, B.W., S.L. Gibbs, B. Chen and M. Savellano, "Fluorescence imaging in vivo: Raster scanned point-source imaging provides more accurate quantification than broad beam geometries," Tech. in Cancer Research & Treatment **3,** 15-21 (2004).
5. Hebden, J.C. and K.S. Wong, "Time-Resolved Optical Tomography," Appl. Opt. **32,** 372-380 (1993).
6. Barbour, R.L., H.L. Graber, J.W. Chang, S.L.S. Barbour, P.C. Koo and R. Aronson, "MRI-guided optical tomography: Prospects and computation for a new imaging method," IEEE Compu. Sc. & Engg. **2,** 63-77 (1995).
7. Pogue, B.W., M.S. Patterson, H. Jiang and K.D. Paulsen, "Initial Assessment of a Simple System For Frequency-Domain Diffuse Optical Tomography," Phys. Med. Biol. **40,** 1709-1729 (1995).
8. Oleary, M.A., D.A. Boas, B. Chance and A.G. Yodh, "Experimental Images of Heterogeneous Turbid Media By Frequency- Domain Diffusing-Photon Tomography," Opt. Lett. **20,** 426-428 (1995).
9. Gonatas, C.P., M. Ishii, J.S. Leigh and J.C. Schotland, "Optical Diffusion Imaging Using a Direct Inversion Method," Phys. Rev. E **52,** 4361-4365 (1995).
10. Ntziachristos, V. and R. Weissleder, "Charge-coupled-device based scanner for tomography of fluorescent near-infrared probes in turbid media," Med. Phys. **29,** 803-809 (2000).
11. Ntziachristos, V., C.H. Tung, C. Bremer and R. Weissleder, "Fluorescence molecular tomography resolves protease activity in vivo," Nat. Med. **8,** 757-760 (2002).
12. Ntziachristos, V., C. Bremer, C. Tung and R. Weissleder, "Imaging cathepsin B up-regulation in HT-1080 tumor models using fluorescence-mediated molecular tomography (FMT)," Acad. Radiol. **9,** 323-325 (2002).
13. Graves, E.E., J. Ripoll, R. Weissleder and V. Ntziachristos, "A submillimeter resolution fluorescence

#6369 - $15.00 US
Received 20 January 2005; revised 19 March 2005; accepted 21 March 2005

molecular imaging system for small animal imaging," Med. Phys. **30,** 901-911 (2003).
14. Graves, E.E., R. Weissleder and V. Ntziachristos, "Fluorescence molecular imaging of small animal tumor models," Current Molecular Medicine **4,** 419-430 (2004).
15. Ntziachristos, V., E.A. Schellenberger, J. Ripoll, D. Yessayan, E. Graves, A. Bogdanov, L. Josephson and R. Weissleder, "Visualization of antitumor treatment by means of fluorescence molecular tomography with an annexin V-Cy5.5 conjugate," Proc. National Academy of Sciences of the United States of America **101,** 12294-12299 (2004).
16. Culver, J.P., R. Choe, M.J. Holboke, L. Zubkov, T. Durduran, A. Slemp, V. Ntziachristos, B. Chance and A.G. Yodh, "Three-dimensional diffuse optical tomography in the parallel plane transmission geometry: evaluation of a hybrid frequency domain/continuous wave clinical system for breast imaging," Med. Phys. **30,** 235-247 (2003).
17. Schulz, R.B., J. Ripoll and V. Ntziachristos, "Experimental fluorescence tomography of tissues with noncontact measurements," IEEE Trans. Med. Imaging **23,** 492-500 (2004).
18. Godavarty, A., M.J. Eppstein, C.Y. Zhang, S. Theru, A.B. Thompson, M. Gurfinkel and E.M. Sevick-Muraca, "Fluorescence-enhanced optical imaging in large tissue volumes using a gain-modulated ICCD camera," Phys. Med. Biol. **48,** 1701-1720 (2003).
19. Godavarty, A., C. Zhang, M.J. Eppstein and E.M. Sevick-Muraca, "Fluorescence-enhanced optical imaging of large phantoms using single and simultaneous dual point illumination geometries," Med. Phys. **31,** 183-190 (2004).
20. Schmitz, C.H., H.L. Graber, H.B. Luo, I. Arif, J. Hira, Y.L. Pei, A. Bluestone, S. Zhong, R. Andronica, I. Soller, N. Ramirez, S.L.S. Barbour and R.L. Barbour, "Instrumentation and calibration protocol for imaging dynamic features in dense-scattering media by optical tomography," Appl. Opt. **39,** 6466-6486 (2000).
21. Ntziachristos, V. and R. Weissleder, "Experimental three-dimensional fluorescence reconstruction of diffuse media by use of a normalized Born approximation," Opt. Lett. **26,** 893-895 (2001).
22. Oleary, M.A., D.A. Boas, X.D. Li, B. Chance and A.G. Yodh, "Fluorescence lifetime imaging in turbid media," Opt. Lett. **21,** 158-160 (1996).
23. Haskell, R.C., L.O. Svaasand, T.T. Tsay, T.C. Feng and M.S. McAdams, "Boundary-Conditions For the Diffusion Equation in Radiative- Transfer," J. Opt. Soc. Am. A - Optics Image Science and Vision **11,** 2727-2741 (1994).
24. Patterson, M.S., B. Chance and B.C. Wilson, "Time resolved reflectance and transmittance for the non-invasive measurement of tissue optical properties," Appl. Opt. **28,** 2331-2336 (1989).
25. Kak, A.C. and M. Slaney, "Principles of Computerized Tomographic Imaging," New York: IEEE Press (1988).
26. Eccles, S.A., W.J. Court, G.A. Box, C.J. Dean and R.G. Melton, "Regression of Established Breast-Carcinoma Xenografts with Antibody-Directed Enzyme Prodrug Therapy against C-Erbb2 P185," Cancer Res. **54,** 5171-5177 (1994).
27. Hillman, E.M.C., D.A. Boas, A.M. Dale and A.K. Dunn, "Laminar optical tomography: demonstration of millimeter-scale depth-resolved imaging in turbid media," Opt. Lett. **29,** 1650-1652 (2004).
28. Dunn, A. and D. Boas, "Transport-based image reconstruction in turbid media with small source-detector separations," Opt. Lett. **25,** 1777-1779 (2000).
29. Li, X.D., T. Durduran, A.G. Yodh, B. Chance and D.N. Pattanayak, "Diffraction tomography for biochemical imaging with diffuse- photon density waves," Optics Letters **22,** 573-575 (1997).
30. Schotland, J.C., "Continuous-wave diffusion imaging," J. Opt. Soc. Am. A - Optics Image Science and Vision **14,** 275-279 (1997).
31. Markel, V.A. and J.C. Schotland, "Inverse problem in optical diffusion tomography. I. Fourier- Laplace inversion formulas," J. Opt. Soc. Am. A - Optics Image Science and Vision **18,** 1336-1347 (2001).
32. Matson, C.L., N. Clark, L. McMackin and J.S. Fender, "Three-dimensional tumor localization in thick tissue with the use of diffuse photon-density waves," Appl. Opt. **36,** 214-220 (1997).
33. Durduran, T., J.P. Culver, M.J. Holboke, X.D. Li, L. Zubkov, B. Chance, D.N. Pattanayak and A.G. Yodh, "Algorithms for 3D localization and imaging using near-field diffraction tomography with diffuse light," Opt. Exp. **4,** 247-262 (1999).
34. Achilefu, S. and R.B. Dorshow, "Dynamic and Continuous Monitoring of Renal and Hepatic Functions with Exogenous Markers," Topics in Current Chemistry. Springer-Verlag: Berlin Heidelberg (2002).
35. Intes, X., J. Ripoll, Y. Chen, S. Nioka, A.G. Yodh and B. Chance, "In vivo continuous-wave optical breast imaging enhanced with Indocyanine Green," Med. Phys. **30,** 1039-1047 (2003).
36. Ntziachristos, V., A.G. Yodh, M. Schnall and B. Chance, "Concurrent MRI and diffuse optical tomography of breast after indocyanine green enhancement," Proc. National Academy of Sciences of the United States of America **97,** 2767-2772 (2000).
37. Cuccia, D.J., F. Bevilacqua, A.J. Durkin, S. Merritt, B.J. Tromberg, G. Gulsen, H. Yu, J. Wang and O. Nalcioglu, "In vivo quantification of optical contrast agent dynamics in rat tumors by use of diffuse optical spectroscopy with magnetic resonance imaging coregistration," Appl. Opt. **42,** 2940-50 (2003).
38. Gurfinkel, M., A.B. Thompson, W. Ralston, T.L. Troy, A.L. Moore, T.A. Moore, J.D. Gust, D. Tatman, J.S. Reynolds, B. Muggenburg, K. Nikula, R. Pandey, R.H. Mayer, D.J. Hawrysz and E.M. Sevick-Muraca, "Pharmacokinetics of ICG and HPPH-car for the detection of normal and tumor tissue using

#6369 - $15.00 US Received 20 January 2005; revised 19 March 2005; accepted 21 March 2005

fluorescence, near-infrared reflectance imaging: A case study," Photochem. Photobiol. **72,** 94-102 (2000).
39. Srinivasan, S., B.W. Pogue, H. Dehghani, S.D. Jiang, X.M. Song and K.D. Paulsen, "Improved quantification of small objects in near-infrared diffuse optical tomography," J. Biomed. Opt. **9,** 1161-1171 (2004).
40. Pogue, B.W., C. Willscher, T.O. McBride, U.L. Osterberg and K.D. Paulsen, "Contrast-detail analysis for detection and characterization with near-infrared diffuse tomography," Med. Phys. **27,** 2693-2700 (2000).
41. Dehghani, H., B.W. Pogue, S.D. Jiang, B. Brooksby and K.D. Paulsen, "Three-dimensional optical tomography: resolution in small-object imaging," Appl. Opt. **42,** 3117-3128 (2003).

1. Introduction

Imaging biochemical events with near infrared fluorescent agents provides an attractive new approach for studying models of human diseases in live small animals. With recent advances in optical probes, and diffuse optical tomography (DOT) methods, quantitative three dimensional assays of probe activity *in vivo* are now feasible. While currently *in vivo* imaging of optical agents is most often accomplished with continuous wave planar reflectance fluorescent techniques [1-3] or raster scanning techniques [4], the newer DOT methods have significant advantages. Quantitative DOT methods account for partial volume effects, reduce the influence of superficial tissues and improve the contrast to noise ratio (CNR) of buried targets [5-9]. Fluorescence DOT images have recently been demonstrated *in vivo* using both fiber-coupled cylindrical geometries [10-12] and lens-coupled planar geometries [13-15]. However challenges remain in the design of real time small animal fluorescence DOT systems that simultaneously provide optimal resolution, sensitivity, full body field-of-view and shorter scan times. The aims of maximizing resolution and field of view emphasize the need for dense spatial sampling, while on the other hand physiological fluctuations, measurement protocols and animal throughput motivate faster imaging speeds. Recent DOT systems have demonstrated the advantages of using a lens to relay light from a tissue surface to a charge-coupled device (CCD) for detection [13, 15-17]. This approach permits dense spatial sampling and large imaging domains on the detected surface. However, previously reported lens coupled CCD systems typically had limited numbers of fiber coupled sources ($N \leq 46$). Source fibers introduce an undesired asymmetry between the illumination plane (sparsely sampled by discrete fibers) and the detection plane (densely sampled by a CCD array detector) and force tradeoffs between sampling density and field of view on the illumination plane. In addition, fiber optic switching times (>0.1 seconds) limit data acquisition speeds. Rather than direct lens coupling, other systems have used arrays of detector fiber to relay light from tissue to a CCD [10-12, 18-20]. While providing source-detector symmetry, this approach does not provide the dense sampling of lens coupled detection.

We present here a fast-scanning (8 Hz per source rate, total whole body scan time ~2.2min), fluorescence DOT system with a 10x larger imaging domain (5 cm x 5 cm x 1.5 cm) compared to an equivalent fiber-switched system while maintaining the same resolution (small object FWHM $\leq$ 2.2 mm) and sensitivity (<0.1 pmole) [13]. The source plane is sampled using flexible, high-density and large field-of-view arrangements by raster scanning a source laser. The fast source switching is complemented by a high frame rate low noise, 5 MHz electron-multiplying CCD camera that increases data acquisition rates by >10x over previous 1 MHz CCD systems. Programmed tissue phantoms experiments were used to establish quantitative calibration, sensitivity, linearity and resolution.

We assess the *in vivo* imaging feasibility and performance of the fast-scanning fluorescence DOT system in studies of nude mice. The effect of probe delivery route is demonstrated by imaging injections of indocyanine green (ICG), a vascular contrast agent, and comparing the kinetics obtained from intravenous injection, versus injection into a fat pocket (retro orbital injection). Feasibility of imaging the distribution of tumor-targeted molecular probes simultaneously in the liver, kidneys and tumors is demonstrated by imaging the uptake of a breast tumor-specific polypeptide in nude mice bearing subcutaneously

#6369 - $15.00 US Received 20 January 2005; revised 19 March 2005; accepted 21 March 2005

implanted human breast cancer carcinoma MDA-MB-361. The polypeptide was conjugated with a near infrared fluorescent probe cypate, which serves as antenna for optical imaging.

2. Methods

Here we describe the fast scanning fluorescence DOT system, including tomographic reconstruction algorithm, experimental system, imaging protocol, data pre-processing, and the protocols for phantom and *in vivo* imaging.

2.1. Image reconstruction algorithms

We reconstruct images of fluorophore concentration by inverting ratiometric data derived from the intensities of the excitation and fluorescence light measured on the detector plane for each source position. The light intensity at the excitation wavelength is written, $\Phi(\mathbf{r}_{s(i)}, \mathbf{r}_{d(i)}, \lambda_{exc})$, where $\mathbf{r}_{s(i)}$, and, $\mathbf{r}_{d(i)}$, are the positions of the ith source and ith detector locations respectively, and λ_{exc} (780 nm) is the excitation wavelength. Similarly, the fluence at the emission wavelength, λ_{emi} (830 nm), is written, $\Phi(\mathbf{r}_{s(i)}, \mathbf{r}_{d(i)}, \lambda_{emi})$. Following the normalized Born approach, formulation of the ratiometric fluorescence/excitation measurements is written in discrete notation as **y=Ax** with the following definitions[21, 22];

$$y_i = \left[\frac{\Phi(\mathbf{r}_{s(i)}, \mathbf{r}_{d(i)}, \lambda_{emi}) - \theta_f \Phi_o(\mathbf{r}_{s(i)}, \mathbf{r}_{d(i),} \lambda_{exc})}{\Phi_o(\mathbf{r}_{s(i)}, \mathbf{r}_{d(i),} \lambda_{exc})} \right] \tag{1}$$

$$A_{i,j} = -\frac{S_o \nu h^3}{D_o} \frac{G(\mathbf{r}_{s(i)}, \mathbf{r}_j, \lambda_{exc}) G(\mathbf{r}_j, \mathbf{r}_{d(i)}, \lambda_{emi})}{G(\mathbf{r}_{s(i)}, \mathbf{r}_{d(i)}, \lambda_{exc})} \tag{2}$$

$$x_j = \partial N_j \tag{3}$$

Here, the two point Greens function, G, models light transport for given boundary conditions and optical properties. Image voxels (x_j) have concentration, ∂N_j and position r_j.

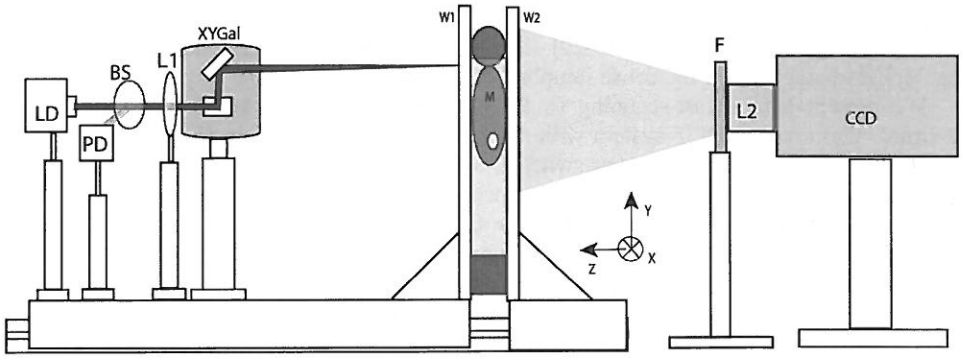

Fig. 1. Fast scanning fluorescence tomography system. The mouse subject is suspended and held in light compression between two movable windows (W1 and W2). Light from a laser diode at 785 nm (LD) is collimated and passes through a 95/5 beam splitter (BS). A reference Photodiode (PD) collects 5% of the beam. The main 95% beam passes through lens (L1) into a XY galvo scanning system (XYGal). The mirror pair scans the beam onto the illumination window (W1) of the imaging tank. Light emitted from W2 is detected by an EMCCD via a filter (F1) and lens system (L2).

#6369 - $15.00 US
Received 20 January 2005; revised 19 March 2005; accepted 21 March 2005

We model the diffuse photon density waves using an extrapolated zero boundary [23], and method of images [24]. Solutions to the slab geometry are used to calculate G [24]. S_o is an empirically determined constant incorporating the filter efficiency, and other wavelength dependent attenuation and gain factors in the system and is obtained through titration experiments. The inverse solution is obtained using algebraic reconstruction technique (ART) [25]. Reconstructions involving 5ART iterations take 7-8 minutes for ~200,000 measurements (~40,000 voxels) using a single processor 3 GHz PC with 2 GB memory.

2.2. Experimental system

A schematic of instrument is shown in Fig. 1 and a picture of the physical system is shown in Fig. 2. The system consists of a source, a scanning mechanism for the source, an imaging tank for the mouse and a CCD camera to collect the light emitted from surface of the imaging tank. Source illumination is provide by a laser diode at 785 nm (Hitatchi, HL785G, P_{ld}=50 mW, temperature stabilized, current regulated). The collimated output of the laser passes through a beam splitter that deflects 5% of the beam to a photodiode for a reference measure of the laser intensity. The remainder of the collimated beam (95% of P_{ld}) passes through a lens (L, focal length 30 cm) into a dual-axis XY galvo system (Model 6230, Cambridge Technology, MA). The galvo system scans the focused illumination (spot size =100 μm) in 2 dimensions over surface of the source plane with a position A to position B switch time of <0.5 ms. The 100 μm source spot size is similar to the multimode fibers sizes used in a wide variety of DOT systems[10-13, 15-20]. The use of the galvanometer mirror pair permits the system to scan an adjustable area of up to 8cm X 8cm with flexible source positioning and source separations. After propagating through the sample volume, transmitted light passes through a selectable filter element and is detected on the opposite plane using a lens coupled CCD camera. A lens coupled, high frame rate EMCCD camera (iXon 877f, Andor Technologies) is used for detection. It provides high dynamic range and high speed acquisition, (TE cooled, 512 x 512 pixels, frame transfer: >35 frames per second , front illuminated, QE 40% @ λ=800 nm, full well 250 K ct, 14 bit, 5 MHz pixel readout, Electron Multiplying (EM) gain stage before the analog to digital conversion with a range of 1-300). The scanning protocol consists of two separate excitation and fluorescence scans. The excitation light intensity profile ($\Phi(\mathbf{r}_{s(i)}, \mathbf{r}_{d(i)}, \lambda_{exc})$) is measured for each source position by placing a neutral density filter (OD=2.0) in the filter position. The fluorescence emission light intensity profile ($\Phi(\mathbf{r}_{s(i)}, \mathbf{r}_{d(i)}, \lambda_{emi})$) is measured by placing an 830 nm narrow band interference filter, 10 nm FWHM (CVI laser Inc.) in the filter position. The excitation and emission images obtained from the EMCCD camera are normalized using the mean source intensity values obtained from the photodiode. This normalization compensates for the differences in light levels between the excitation and emission scans. A full frame 4x4 binned image data (128 x 128) is collected for all the source positions. The full detector images are cropped and binned to generated set of detector measurement positions symmetrically arranged in the x-y plane such that for x-y source position there is a matched x-y detector position. For example, for a 24 x 36 grid of source positions with 2 mm spacing, the source plane is sampled over a 48 mm x 72 mm, region (x=-24 mm to 24 mm, y=-36 mm to 36 mm). From the detectors images, the same xy plane, 48 mm x72 mm, region of interest (x=-24 mm to 24 mm, y=-36 mm to 36 mm) was extracted from each image collected for each source position. The cropped images are then binned with into a 24 x 36 grid of 2 mm x 2 mm bins. Thus for each source position a 24 x 36 grid of binned detectors are obtained, and reciprocally for each detector position a grid of 24 x 36 source positions are illuminated. In this example a total of 864 sources and 864 detectors are acquired, for a total of 746496 source-detector pairs.

#6369 - $15.00 US
Received 20 January 2005; revised 19 March 2005; accepted 21 March 2005

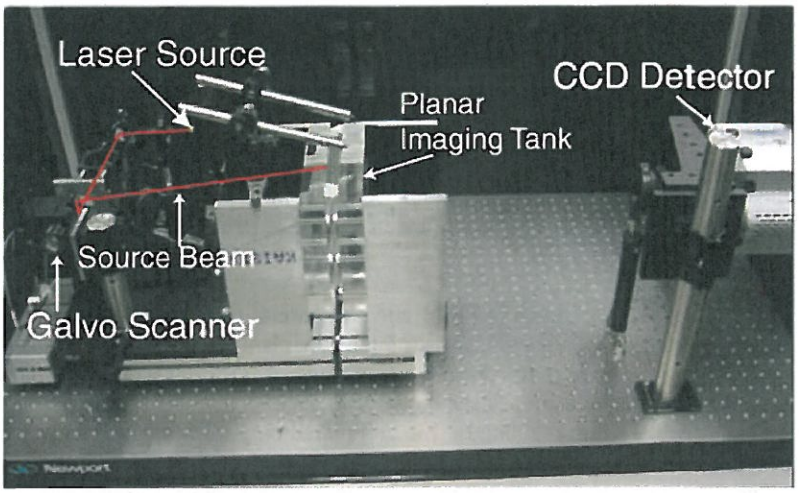

Fig. 2. Small animal fluorescence DOT system. The mouse subject is suspended between two movable windows. Light from a near infrared laser diode (785 nm) is scanned by a mirror pair on to the illumination window of the imaging tank. Fluorescing light emitted from the opposing window is detected by a lens coupled EMCCD Camera after passing through a filter that rejects the excitation light. CCD images are acquired for each source position. The full data set is then inverted to provide tomographic images of the concentration of exogenous fluorescing agents.

2.3. Phantom imaging protocol

The sensitivity and calibration of the system was assessed using tissue phantoms. The imaging tank was filled with a matching fluid (Intralipid™, water, and, India ink, for μ_a=0.3 cm^{-1}, μ_s'=10 cm^{-1}). Targets were prepared using 3 mm diameter plastic tubes that were filled with ICG concentrations ranging from 1 nM to 1 μM, and the matching fluid. The tubes were attached to a phantom holder and placed at the center of the imaging tank. Excitation and emission scans were taken using a 48 x 16 array with 1mm square spacing between the adjacent source positions(x=-24 mm to 24 mm, y=-8 mm to 8 mm). The data was reconstructed using the procedures outlined above to generate three dimensional tomographic images. Volume averaged values of the raw images were compared to the known concentrations to evaluate sensitivity, linear and to determine S_0. The spatial resolution of the system was evaluated by imaging two tubes with inside diameter=1.6 mm, containing a 1 μM solution of ICG and matching fluid. The tubes were arranged in the imaging tank at the same distance, z_{target} from the detection plane and displace by 24 mm in the x direction. A micrometer attached to the phantom holder was used to vary the z_{target} position. Data was acquired with z_{target} = {2.5, 5, 7.5, 10, 12.5} mm. Following image reconstruction, the FWHM values of the tubes were obtained from the 3D reconstructions by analyzing cross sectional traces.

2.4. In vivo imaging protocol

All in vivo studies were performed in compliance with the Washington University Animal Study Committee's requirements for the care and use of laboratory animals in research. For small animal imaging, anesthetized nude mice (ketamine/xylazine via intraperitoneal injection) were suspended between the source and detector windows. A matching fluid (μ_a=0.3 cm^{-1}, μ_s' = 10 cm^{-1}) surrounds the animal. With warmed matching fluid (T=38 °C), the mice can be imaged multiple times over the normal course of anesthetic dose (30-60 min). The full protocol for a combined fluorescence/excitation scan (a 24 x 36 array with 2 mm

#6369 - $15.00 US
Received 20 January 2005; revised 19 March 2005; accepted 21 March 2005

square spacing between source positions, x=-24 mm to 24 mm, y=-36 mm to 36 mm) took 5-6 minutes including animal positioning, emission and excitation scanning, retrieval of animal from the scanner and reconstructing the data.

2.5. Vascular agent kinetics

An anesthetized (ketamine/xylazine via intraperitoneal injection) mouse was suspended between the source and detector windows and was injected retro-orbital (RO) with a dosage of 0.3 μmol (100 μL) per kg body weight of mouse of ICG in 20% aqueous DMSO solution. The RO injection protocol, consisted of carefully introducing the tip of a 27 gauge hypodermic needle in front of the eye with the needle bevel oriented away from the eye surface. Solutions injected at this site are rapidly taken up taken up by the capillary nexus. Our scanning protocol involved taking a single excitation scan followed by 5 consecutive emission scans. The procedure was repeated for 1 hour, finishing with a final excitation scan. Interpolated excitation scans were generated at the times appropriate to each fluorescence scan using the two temporally nearest excitation scans. The ratiometric data, y in Eq. (1), was generated using the emission and interpolated excitation scans at each time point. The emission measurements are wholly dependent on ICG concentration, while the excitation measurements are only slightly modulated (≤10%), even at the highest concentrations. The 5:1 emission–to-excitation scanning procedure was chosen to provide greater scanning time for the more sensitive emission measurements, while still accounting for the small changes in the excitation scan.

Measurements were also conducted for a mouse with intravenous (IV) administration of ICG. In this case, before placing the mouse in the scanner, 100 μL of ICG (0.3 μmol/kg body) was administered IV in the tail vein. The mouse was positioned in the scanner and imaged continuously for 1 hour using the same parameters described above. For both studies, volumes of interest were identified for the kidneys, liver, shoulder and head using the anatomical pictures of the subjects. The mean fluorescence intensity from these volumes were then calculated and plotted as a function of time.

2.6. Tumor imaging with targeted probe

Tumor imaging was evaluated using subcutaneously implanted human MDA MB 361 breast carcinoma xenografts in nude mice. This tumor cell line is widely used as a human breast cancer model [26]. The molecular probe is based on a polypeptide that targets breast-specific proteins in the tumor cells and cypate serves as optical NIR antenna for localizing the probe's distribution *in vivo*. Nude mice (18-22 g) were anesthetized with xylazine/ketamine cocktail via intraperitoneal injection and placed in a supine position. The mice were injected subcutaneously in the lower back of the mice with 1 x 106 MDA MD 361 cells. Tumor masses were palpable at 5 weeks post implant, which reached 5 mm in 5-8 weeks. Prior to injection of the molecular probe, the mice were anesthetized as described above. The probe dissolved in 20% aqueous DMSO and animals were injected retro-orbitally with doses of 0.3 μmol/kg body weight using a 29 gauge needle. The mouse was scanned 24 hours post delivery of the contrast agent.

3. Results

3.1. System performance evaluation

Figure 3 shows the graph of concentration of ICG vs. reconstructed signal, obtained from the ICG titration measurements. The data demonstrate that the present fluorescence DOT system has a sensitivity of 1 nM concentration (100 fmole) and provides a linear measure from 1 nM to 1 μM concentrations of the fluorescent agent. Figure 3 also shows the noise floor of the camera without using the EMCCD gain; this indicates the sensitivity limit without EM gain. The EM gain reduces the effective read-out noise and improves the system sensitivity.

#6369 - $15.00 US
Received 20 January 2005; revised 19 March 2005; accepted 21 March 2005

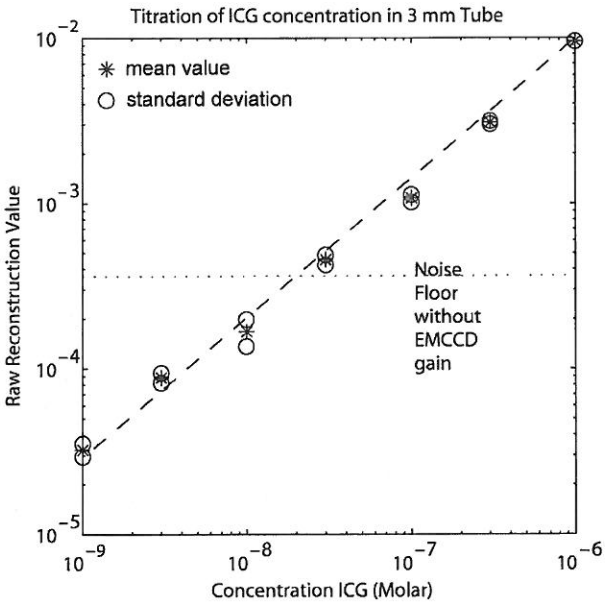

Fig. 3. Calibration and Sensitivity. Known concentration –vs- raw reconstruction values for titrations of ICG in 3 mm tube phantoms. The data establish a calibration coefficient, and establish the region of linear response.

To account for the potential partial volume effects, the calibration factor S_0 was obtained by integrating the raw images and the known concentrations of ICG over a 1 cm x 1 cm x 1 cm volume encompassing the tube phantom. The calibration factor S_0 is defined as $S_0 = CR/Rs$, where Rs is the volume average of the raw reconstructed values, and CR is the volume average of the known ICG concentration.

The set-up used to characterize system resolution is shown in Fig. 4(a). A sample image for the z_{target}=8.5 mm is shown in Fig. 4(b). From the reconstructions, the full width half maximum (FWHM) was calculated as a function of depth (Fig. 4(c)). The data demonstrate that, for a target with physiologically relevant amount (100 pmole) of fluorescent probe, the system can report a FWHM=2.25 mm near the source and the detector planes and FWHM=2.75 in the middle of the tank at a depth of 7.5 mm.

3.2. Biodistribution and probe dynamics measurements

A mouse was scanned after retro-orbital delivery of ICG over a period of ~1 hour. Figure 5 shows the 2D slices obtained from the 3D reconstruction at various depths from the detector plane 3 minutes after the probe delivery. Slice distances are measured from back of the mouse on the detector plane. Localization of ICG in the two kidney shapes is evident in the 4.5 mm slice (arrows) while, elevated ICG contrast in a single liver shape is evident in the 10.5 mm slice (arrow). The 7.5 mm slice shows the retro orbital site of ICG administration. Using the anatomical picture of the mouse and the 2D reconstruction slices (Fig. 5) as a guide; volumes of interest (VOI's) were selected corresponding to the liver, kidneys, shoulder and brain. The mean probe concentrations were calculated for these VOI's for all time points. Figure 6 shows the anatomical picture of the mouse with the selected positions for VOI's marked on it. Mouse anatomy was used to select the third dimension for the VOI's. For the liver, kidneys, head and shoulder, slices 7 mm -13 mm, 2 mm – 7 mm, 5 mm – 10 mm and 5 mm – 10 mm

#6369 - $15.00 US
Received 20 January 2005; revised 19 March 2005; accepted 21 March 2005

were used respectively. Figure 7(a) shows the time course of ICG in each VOI for retro-orbital injection. Clearly, ICG is accumulating in the liver, while rem aining constant or slowly clearing from the other tissues.

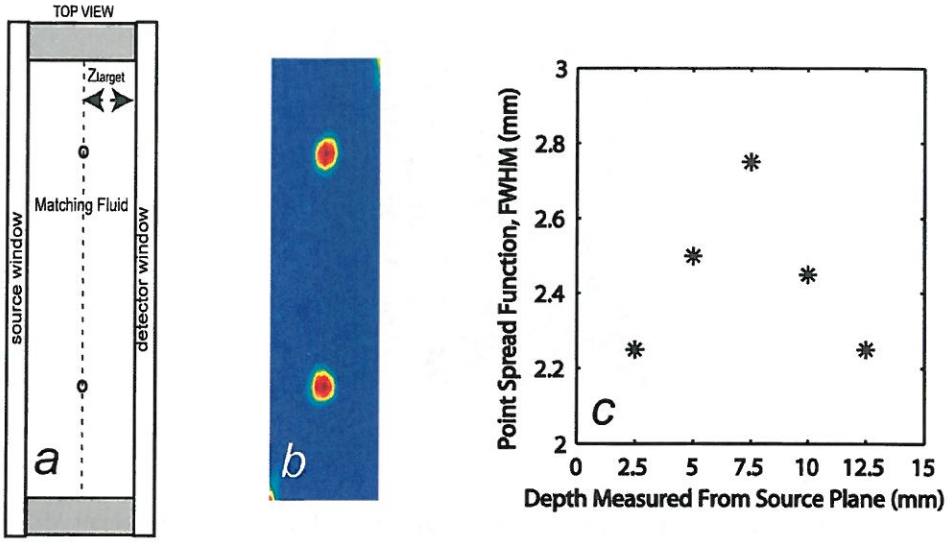

Fig. 4. Resolution vs depth. a) Phantom measurement set-up. Depth of the phantom z_{target} is measured from the detection plane. b) A xz plane slice at y=0 from a reconstructed volume of two 1.6mm diameter tubes (with 0.1 μM ICG). c) Full width half maximum (FWHM) Vs. Depth measured from the detection plane.

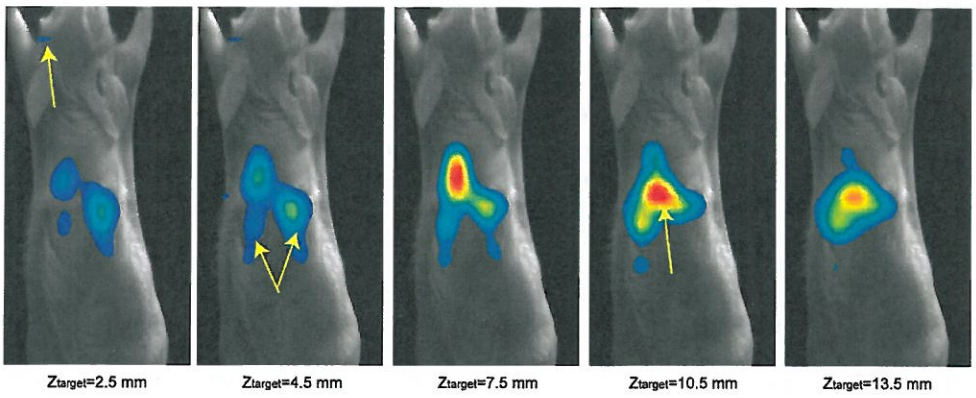

Fig. 5. Biodistribution of indocynaine green (ICG) 3 min after retro orbital injection. 2D slices obtained from the 3D reconstruction are shown at various depths, z_{target} , from the detection plane. The arrows indicate the site of ICG administration (Retro Orbital) z_{target}=2.5, kidneys for z_{target}=4.5, and the liver z_{target}=10.5. Note the localization of ICG in the liver as compared to the kidneys 3 minutes after the probe delivery.

Probe dynamics were also obtained for ICG using IV administration and compared with the retro-orbital (RO) method. Figure 7(b) shows the time course comparison between IV and RO delivery obtained from the VOI for the liver. IV administration delivers the agent more quickly to the liver compared to RO administration. After 30 minutes, ICG liver levels

#6369 - $15.00 US
Received 20 January 2005; revised 19 March 2005; accepted 21 March 2005

approached similar levels for both administration methods. Figure 5 and Fig. 7 demonstrate the feasibility of using fluorescence DOT for pharmacokinetic studies and evaluating dynamic experimental models.

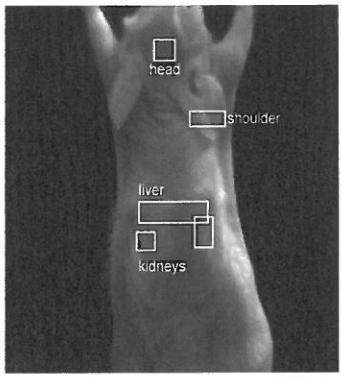

Fig. 6. Volumes of interest used for head, shoulder, liver, and kidneys in the x-y plane.

3.3. Tumor targeted fluorescence agents

An animal model with a subcutaneous breast-specific human breast cancer xenograft MDA MD 361 was used to evaluate the localization of a molecularly targeted probe. Figure 8 shows a 2D slice parallel to the detector plane at a depth of z = 2.5mm and a 2D slice extending from the source plane to detector plane at y = 12mm, obtained from the 3D tomographic reconstruction. The tumor (breast cancer) shows uptake of a fluorescing near infrared cypate derivative probe with a poly peptide that targets a protein receptor expressed in breast cancer. The kidneys also show contrast. The maximum values of probe concentration obtained from the tumor, liver and kidney volumes as a ratio of the background are 54.7, 32.4, and 58.3 respectively.

4. Discussion

The objective of the current fluoro-DOT system is to provide a means for imaging the spatio-temporal evolution of fluorescent probe distributions *in vivo*. A system that simultaneously provides optimal resolution, sensitivity, full body field-of-view and short scan times would provide valuable information about probe kinetics, retention, clearance pathways and localization of optical molecular probes. The fluoro-DOT system presented here extends on previous DOT systems to address this imaging need.

Previous planar geometry DOT systems based on lens coupled CCD detection employed limited numbers of sources and therefore a compromise between the field of view and spatial sampling density on the source plane was required. For example, a previously reported fiber based CCD system designed for breast imaging with a planar geometry, used 45 source positions. The sources were arranged in a 9x5 grid with 1 cm spacing covering an 8x4 cm field of view [16]. In another example, a fiber based small animal fluorescence DOT system employed 32 fixed source positions [10]. Although, the detection planes of these systems had dense spatial sampling, the source planes were sampled with roughly 1-3 orders of magnitude smaller optode counts.

#6369 - $15.00 US
Received 20 January 2005; revised 19 March 2005; accepted 21 March 2005

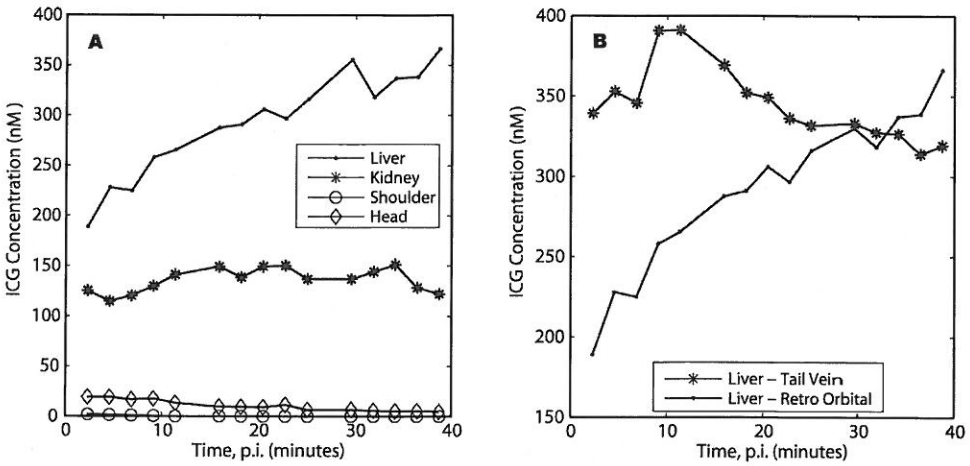

Fig. 7. Temporal kinetics of ICG. a) Time course of ICG distribution for retro-orbital injection in ROI's for liver, kidney, head and shoulder. b) Time course comparison for ICG between IV and Retro Orbital delivery.

The present system, in contrast, uses a raster scanning lens coupled source for flexible dense spatial sampling. The spot size at the source is 100 μm, and the accessible imaging domain is 8x8 cm, providing, in principle, 640,000 possible source positions. On the detection side the raw 512x512 CCD pixel count provides similar spatial sampling (262,000 pixels). While the imaging examples shown in this report used 1 or 2 mm source and detector sampling, we note that the system is capable of the much higher resolution ~100 μm source sampling. When imaging tissues close (<3 mm) to the source and detector planes dense sampling with ~100 μm capability may be useful [27, 28]. In addition, for large numbers of source positions the raster scanning solution is more cost effective than a fiber optic switch. Epi-illumination from the detector side, though not presented herein, is also possible with the present setup. The source can be directed around to the detector plane for raster scanning and reflectance tomography. Alternatively the beam could be expanded for planar reflectance illumination, providing both fluorescence tomography and fluorescence reflectance imaging within a single system [13].

Another challenge for fluorescence tomography is speed. Imaging rates are limited by both the control aspects of source multiplexing, data acquisition, and by the available signal to noise levels. Our design addresses the multiplexing issue by decreasing the switch time from 250 ms between sources (for fiber optic switch) to <1 ms for galvo scanning, and using an EMCCD with a high speed 5MHz readout. To take full advantage of the increased control speed, it is desirable to also decrease noise levels. Use of the EMCCD achieves this by reducing the effective readout noise from $45e^{-1}$ rms to ~$1e^{-1}$ rms, while maintaining the dynamic range of the camera. This is evident in the sensitivity curve (Fig 3.). The detection threshold of our system is 1 nM of ICG, measured using a 3 mm diameter tube phantom located at the center of the imaging volume (depth of 7.5 mm from the detector window). Comparisons with other systems can be complicated by the wide variety experimental and data processing details including, approaches to system design, forward calculations, inversion strategies, details such as voxel counts, measurement numbers, source and detector sizes and positions, signal to noise ratios, phantom test specifics, and metrics of image quality. Nonetheless it is instructive to compare our results to several recent reports. The results of our instrument sensitivity are similar to the results (1 nM, and ~200 fmole) previously reported for both a fiber coupled cylindrical geometry system[10] and lens coupled planar geometry system[13]. Other studies with frequency domain systems have

#6369 - $15.00 US
Received 20 January 2005; revised 19 March 2005; accepted 21 March 2005

demonstrated images of larger targets (>3 mm) with higher concentrations (>100 nM) though the sensitivity limits were not reported for comparison with measurements reported here[18]. Figure 3 shows the calibration-sensitivity graph obtained using phantom measurements for our system. While the noise floor for a CCD camera without EM gain would limit the detection threshold to ~ 20 nM, with the EMCCD our system has a 1nM detection threshold.

In addition to data acquisition rates, image reconstruction computation times are also important to consider. The large data sets acquired with this system become challenging to reconstruct. With the presented ART reconstruction methods, data inversion requires substantially more time than data acquisition. However, the planar geometry used for this system is particularly amenable to faster analytic inversion procedures such as diffraction tomography[29-33]. Application of these methods could substantially reduce data inversion times.

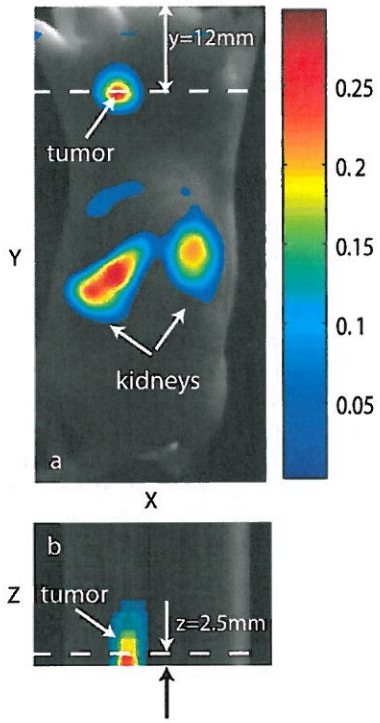

Fig. 8. Representative slices from a 3D tomographic reconstruction of a nude mouse with a subcutaneous breast-specific human breast cancer xenograft MDA MD 361. a) a xy slice parallel to the detector plane at a depth of z = 2.5mm and b) a xz slice extending from the source plane to detector plane at y = 12mm.

While increasing the field of view (5 cm x 5 cm x 1.5 cm) and reducing the data acquisition time (scan time < 2.2min), we have also maintained the resolution of the system at par with recent small animal fluorescence DOT systems [10-15, 17]. Our system can report a FWHM that ranges from FWHM=2.25 mm at a distance 2.5 mm from either the source or detector planes, to FWHM=2.75 mm in the middle of the imaging domain at a distance 7.5 mm measured from either plane. We note that there are various methods of reporting resolution in the literature. The FWHM values are conservative estimates that do not incorporate a deconvolution of the size of the actual objected from the imaged object. In our

#6369 - $15.00 US
Received 20 January 2005; revised 19 March 2005; accepted 21 March 2005

system we image a line object of diameter 1.6 mm with contrast to noise ratio (CNR) >3:1 in the reconstructed images. Using a similar FWHM approach, a fiber coupled cylindrical system reported in Ref [10] has a spatial resolution of 1 mm near the surface and 2.8 mm at the center of the imaging volume while using 1.5mm capillary tube containing 800 nM of Cy5.5 dye. The lens coupled planar geometry system reported in Ref [13] uses 3 mm diameter tubes filled with 2 μM solution of Cy5.5 and is able to separate the tubes with edge to edge separation of 0.7 mm and center-to-center distance of 4.3 mm.

Our study of ICG kinetics (Figs. 5-7) demonstrates the capability of the system to monitor the spatio-temporal evolutions of probe bio-distribution *in vivo*. First we report that operationally the matching fluid is a viable approach. Positioning the animal is quick and high throughput procedures, with ~10 mice per hour are feasible. While the matching fluid adds an additional step to the imaging, the procedure is simple and without complications.

Three dimensional probe distributions are depicted for a single time frame at 3 minutes following retro orbital (RO) delivery (Fig. 5). Due to the large field of view, simultaneous quantitative imaging of the tumor, kidneys, liver and other organs is possible. Figure 7 shows capability of the system to quantitatively tracking the changes in the probe concentration in different organs and regions of the body as a function of time. A RO injection initially deposits the ICG into a fatty pocket behind the eye. ICG then slowly diffuses into the blood stream over the next 20-30 minutes. Traces of the ROI's for the head and shoulder in Fig. 7 indicate the concentration in the blood stream, which is decaying slowly over the course of an hour. At the same time the ICG concentration in the liver steadily increases over the first hour. The kidney shows a somewhat steady value with a slow decay towards the end of the hour. These observations are consistent with the known hepatic clearance pathway of ICG [34]. The ICG concentration in the kidneys is somewhat more elevated than the shoulder or head as expected for a small amount of accumulation in the kidney. This temporal resolution is sufficient for pharmacokinetics and pharmacodynamics studies with time scales on the order of minutes.

Figure 7(b) also compares the ICG kinetics obtained from the two methods of administration namely, RO and IV. When administered intravenously, ICG rapidly binds to plasma proteins and is exclusively cleared by the liver, and subsequently secreted into the bile [34]. Comparing RO with IV administration, the liver uptake kinetics is much faster with the IV method due to direct administration in to the blood stream.

ICG has been explored as a optical contrast agent for *in vivo* imaging by several research groups. In humans, ICG has been used for contrast enhancement of breast cancer tumors [35, 36]. DOT images were shown to co-register accurately with dynamic MRI images[36], and a two compartment model has been used to analyze ICG pharmacokinetics [35]. In animal studies, the kinetics of ICG and methylene blue (MB) were compared using combined frequency domain and steady-state optical spectroscopy techniques [37]. MB, as a smaller molecular weight contrast agent, was more sensitive to blood flow and the arterial input function. ICG, because of its binding to plasma proteins, behaves as a macromolecular contrast agent and was used quantify physiologic parameters related to capillary permeability. In other studies, frequency domain fluorescent reflectance images of ICG and HPPH-car were evaluated for discriminating spontaneous canine adenocarcinoma from normal tissue [38].

While ICG is a useful vascular contrast agent, probes that report on molecular interactions and physiological processes offer much more powerful imaging strategies. Previous studies have shown that cypate have similar photophysical, excretion and blood clearance profiles as ICG [1]. Unlike ICG, cypate has the ability to react with bioactive molecules. This allows its delivery to target tissues by conjugating the fluorescent dye with biological carrier. As shown in Fig. 8, the breast tumor-specific cypate-polypeptide molecular probe localizes efficiently in the tumor tissue. Apart from the kidneys, which are the major excretion organ of the molecular probe, the DOT image showed a high selectivity of the probe in tumor tissue, relative to surrounding tissues. Thus, the fast-scanning DOT system provides

#6369 - $15.00 US Received 20 January 2005; revised 19 March 2005; accepted 21 March 2005

a reliable approach to screen the effectiveness of novel molecular probes in small animals. Note that the wide FOV reports the probe concentration throughout the mouse body. In this example we used a probe that provides optimal localization at 24 hrs p.i.. With the faster imaging performance of the presented fluorescence DOT system, it would be possible to use probes with faster uptake and clearance kinetics. Potentially, the entire temporal kinetics can be used for localizing biological activity rather than single time point images.

The tumor volume imaged in Fig. 8 has an imaged volume of approximately 27 uL, peak concentration of 90 nM and an integrated 2.43 pmole of cypate probe. Previous studies of object sizes by DOT, have shown that for objects smaller than the FWHM of the effective point spread function (PSF), the peak signal drops significantly [16, 39-41], as expected due to partial volume considerations. However, the integrated contrast, summed over a volume larger than the PSF-FWHM, remains much closer to the expected value than comparisons of peak value [16, 39]. The current system has a PSF with FWHM in the range of 2-3 mm. Tumors that are smaller than the tumor in Fig 8, would provide similar contrast provided the integrated cypate-probe concentration over the entire tumor volume were to remain equivalent.

5. Conclusions

The combination of a raster scanning laser source and EMCCD detection provides a simple, flexible, and symmetric planar DOT system. The preliminary phantom and *in vivo* results presented herein demonstrate feasibility of providing quantitative whole body biodistribution assays of molecularly targeted fluorescent probes. The system images probe dynamics on minute time scale, making feasible real-time studies of: pharmacokinetics, pharmacodynamics, disease progression, therapy, and other dynamic experimental models.

Acknowledgments

The authors acknowledge financial support from, National Institutes of Health, K25-NS44339 (JPC), BRG-1 R01 CA109754 (SA), Small Animal Imaging Resource Program (SAIRP) grant, R24 CA83060 (JPC,SA), Department of Defense DAMD-17-0210613 (SA) and the National Science Foundation, BES011948 (SA).

#6369 - $15.00 US Received 20 January 2005; revised 19 March 2005; accepted 21 March 2005